

Spin waves parametrically excited via three-magnon scattering in narrow NiFe strips

Genki Okano¹ and Yukio Nozaki^{1,2,*}¹*Department of Physics, Keio University, Yokohama 223-8522, Japan*²*Center for Spintronics Research Network, Keio University, Yokohama 223-8522, Japan*

(Received 13 May 2019; revised manuscript received 25 July 2019; published 18 September 2019)

Three-magnon scattering can be used to evaluate the lowest frequency of the magnon band in a ferromagnet. Both the ferromagnetic-resonant (FMR) frequency f_{FMR} and the lowest frequency of the magnon band f_{min} in narrow-shaped NiFe strips were electrically measured using the anisotropic-magnetoresistance effect. The comparison with a micromagnetic simulation shows that f_{min} of the magnon band can be controlled independent of f_{FMR} by varying the width w and thickness t of the NiFe strip while maintaining a constant t/w ratio. In addition, we found that the frequency difference, $f_{\text{FMR}} - f_{\text{min}}$, can be greatly increased in thicker NiFe strips. Our results show that narrow-shaped ferromagnets allow us to tune the magnon-band structures by varying their w and t . This ability is important for designing magnon circuits in integrated magnonic devices and for improving the quantitative study on the Bose-Einstein condensation of magnons.

DOI: [10.1103/PhysRevB.100.104424](https://doi.org/10.1103/PhysRevB.100.104424)

I. INTRODUCTION

Spin waves are potential candidates for realizing ultrafast, low-power digital-data processing because they provide a Joule-heating-free transfer of spin information over a sub-millimeter distance in insulating magnetic materials such as $\text{Y}_3\text{Fe}_5\text{O}_{12}$ [1]. The scientific research field concerned with information transport and processing by spin waves is known as magnonics [2,3]. Various magnonic devices have been proposed to date, including logic gates [4–8], majority gates [9,10], interferometers [11–13], transistors [14,15], and others [16–18]. It is known that magnons can form a Bose-Einstein condensate (BEC), even at room temperature [19–24]. Consequently, magnon supercurrent has attracted considerable attention owing to the ability to realize an ultralow-power-consumption transfer of digital information [24–26].

In magnonics, the engineering of a magnon-band structure is significant because it determines both the linear and nonlinear behavior of magnons. A promising approach to control the magnon-band structure is to utilize magnonic crystals [1,27–30], which are artificial periodic magnetic materials. In such periodic structures, Bragg scattering affects the spin wave spectrum and results in the formation of band gaps. However, the ability to tune the magnon-band structure in a confined ferromagnetic element is important to realize integrated magnonic devices. Magnon bandwidth can be roughly defined as $\Delta f \equiv f_{\text{FMR}} - f_{\text{min}}$, where f_{FMR} and f_{min} are the ferromagnetic-resonant (FMR) frequency and the minimum frequency of the magnon-band structure, respectively. From the analytical equation, which provides the magnon dispersion relationship for the thin-film limit, it is expected that the width of Δf is only a few gigahertz.

In this paper, we demonstrate that Δf can considerably vary compared with the thin-film-limit case. To obtain Δf , we

experimentally measured f_{FMR} and f_{min} by observing parametric magnons, which were excited via the three-magnon scattering process in which one magnon with $(f, k) = (f_{\text{ac}}, 0)$ splits into two magnons with $(f_{\text{ac}}/2, \pm k)$. We can evaluate f_{min} of the magnon-band structure because three-magnon scattering occurs only when $f_{\text{ac}}/2 > f_{\text{min}}$. We detected the three-magnon scattering spectra using an electric method based on the measurement of the anisotropic-magnetoresistance (AMR) effect. The large decrease in f_{min} from f_{FMR} (i.e., the large Δf) appeared especially for narrow NiFe strips, and the amplitude of Δf was sensitive to the width w and thickness t values of the NiFe strips even when the aspect ratio t/w was fixed. The results enable us to change Δf by fixing f_{FMR} because f_{FMR} has the same value at a given t/w . From an application point of view, the wide and tunable Δf is favorable for designing magnonic devices. Furthermore, from a fundamental point of view, the magnon-band structure must be systematically controlled to study the BEC of magnons. Recently, it was reported that there are multiple channels for parametrically excited magnons to be transferred toward a condensed state [21,24]. However, it is difficult to explore the complicated condensation process in the $\text{Y}_3\text{Fe}_5\text{O}_{12}$ film, which is generally used to study the BEC of magnons, because the magnon-band structure cannot be considerably changed in thin films. Our findings show the magnon-band structure can be greatly deformed by changing only the width and thickness of a ferromagnetic strip without changing the material, which allows us to completely understand the BEC of magnons.

The remainder of this paper is organized as follows. Section II briefly introduces the scheme for three-magnon scattering. The experimental setup and results are presented in Sec. III. Section IV describes the numerical simulation results of the magnon-band structure, and we compare the experimental and numerical results. The conclusions are presented in Sec. V.

*Corresponding author: nozaki@phys.keio.ac.jp

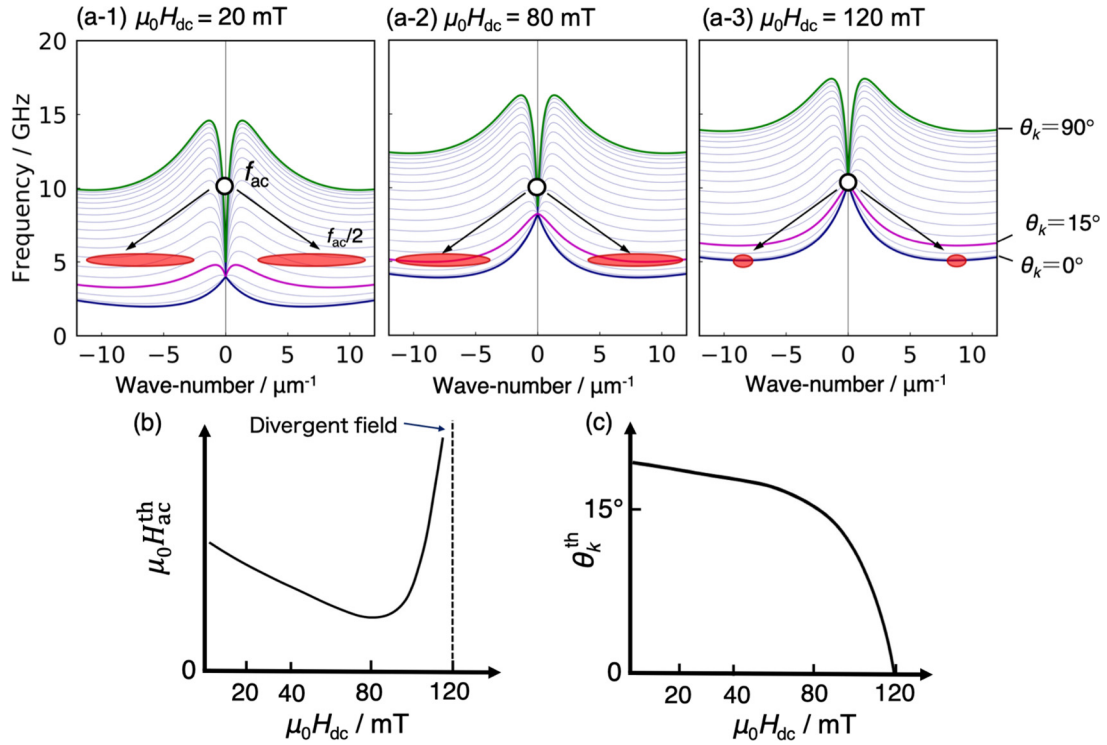


FIG. 1. Schematic illustration of the three-magnon scattering process in the magnon-band structure. (a) Magnon-band structures calculated for the 60-nm-thick NiFe film at (a1) $\mu_0 H_{dc} = 20$ mT, (a2) 80 mT, and (a3) 120 mT. The blue (green) thick solid line shows the dispersion curve for the BVW mode with $\theta_k = 0^\circ$ (MSSW mode, $\theta_k = 90^\circ$). The thin gray solid lines show the dispersion relationship of the magnons with oblique wave vectors at an interval of 5° ; the solid magenta lines show the dispersion relationship for $\theta_k = 15^\circ$. The black open circles indicate the uniform magnons, which were forcibly excited by the microwave field; the magnons scattered via three-magnon scattering are indicated by red ellipses. (b) Schematic magnetic field dependence of $\mu_0 H_{ac}^{th}$ (i.e., a butterfly curve). (c) Magnetic-field dependence of the critical propagation angle θ_k^{th} , which gives $\mu_0 H_{ac}^{th}$.

II. THREE-MAGNON SCATTERING AND THE THRESHOLD CONDITION

Here, we introduce the principle of three-magnon scattering, which is applicable for a thin-film configuration [31]. For a ferromagnetic rectangle with $t/w \ll 1$, the spin wave dispersion relation is generally approximated by the following equations [32–36]:

$$f(k) = \frac{\gamma}{2\pi} \sqrt{\left[\mu_0 H_{dc} + \frac{2A}{M_s} k^2 \right] \left[\mu_0 H_{dc} + \frac{2A}{M_s} k^2 + M_s F_p(kt) \right]}, \quad (1)$$

$$F_p(kt) = 1 - N(k) \sin^2 \theta_k + \frac{M_s}{\mu_0 H_{dc} + \frac{2A}{M_s} k^2} [N_k(1 - N_k)] \cos \theta_k, \quad (2)$$

$$N_k = (1 - e^{-kt}) / (kt), \quad (3)$$

where $F_p(kt)$ is the dipole-interaction factor. Here, γ , M_s , and A are the gyromagnetic ratio, saturation magnetization, and exchange-stiffness constant, respectively. θ_k is the relative angle between the magnetization vector and the wave vector \mathbf{k} of the spin waves. Figures 1(a1)–1(a3) show the examples of the magnon bands, which are calculated on the basis of Eq. (1) for a 60-nm-thick NiFe at $\mu_0 H_{dc}$ of 20, 80, and 120 mT, respectively. The blue and green solid lines in Figs. 1(a1)–1(a3) show the dispersion relationships of the magnetostatic

backward-volume wave (BVW; $\theta_k = 0^\circ$) and magnetostatic surface wave (MSSW; $\theta_k = 90^\circ$), respectively. The other thin solid lines show the dispersion relationship for oblique wave vectors at an interval of 5° . Here, a microwave field with a frequency f_{ac} of 10 GHz is assumed, and the black open circles represent the forcibly excited magnons with $(f_{ac}, k) = (10 \text{ GHz}, 0)$. When the pumping microwave field is beyond the threshold value, the higher-order spin wave interactions lead to exponential growth of various magnon pairs with opposite wave vectors [33,34,36]. As schematically shown in Fig. 1(a), three-magnon scattering is the process by which one magnon with $(f_{ac}, k = 0)$ splits into two magnons with $(f_{ac}/2, \pm k)$, which are represented by the red ellipses. In particular, three-magnon scattering occurs only when $f_{ac}/2 > f_{min}$. The amplitude of the ac magnetic field $\mu_0 H_{ac}$ must be larger than the threshold value $\mu_0 H_{ac}^{th}$, which depends upon both the k and θ_k values of scattered magnons with $f_{ac}/2$. For the thin-film configuration [33], $\mu_0 H_{ac}^{th}$ is analytically written as

$$\mu_0 H_{ac}^{th} = \frac{f_{ac}}{f_M} \min_{k, \theta_k} \left\{ \frac{1 - \left(\frac{f_{FMR}}{f_{ac}} \right)^2 \frac{\Delta \mu_0 H_k(k, \theta_k)}{\sin \theta_k \cos \theta_k}}{1 + \frac{f_{FMR}}{f_{ac}} e_k(\theta_k)} \right\}, \quad (4)$$

where $\min_{k, \theta_k} \{g(k, \theta_k)\}$ represents the minimum value of $g(k, \theta_k)$ with respect to k and θ_k . f_M and f_{FMR} are γM_s and

the FMR frequency,

$$f_{\text{FMR}} = \frac{\gamma}{2\pi} \sqrt{[\mu_0 H_{\text{dc}} + (N_y - N_x)M_s][\mu_0 H_{\text{dc}} + (N_z - N_x)M_s]}, \quad (5)$$

where N_x , N_y , and N_z are demagnetizing factors along the x , y , and z axes, respectively. $e_k(\theta_k)$ is the k -dependent ellipticity of the magnetization precession. $\Delta\mu_0 H_k$ is the spin wave linewidth parameter, which is empirically written as $\Delta\mu_0 H_k(k, \theta_k) = A_0 + A_1 k + A_2 \sin^2 2\theta_k$, where A_0 , A_1 , and A_2 are the coefficients. It is known that the empirical equation can explain well the experimental results for the yttrium iron garnet sphere and NiFe film cases [31,33]. Although it is difficult to obtain the explicit k and θ_k dependences of $\Delta\mu_0 H_k$ and $e_k(\theta_k)$, it has been experimentally determined that the function in the curly brackets in Eq. (4) reaches its minimum at approximately $\theta_k = 15^\circ$ [31], as shown in Fig. 1(a) by the solid magenta lines.

Figures 1(b) and 1(c) show the schematic $\mu_0 H_{\text{dc}}$ dependence of $\mu_0 H_{\text{ac}}^{\text{th}}$ and the corresponding critical propagation angle θ_k^{th} , respectively, which can be explained by considering the dispersion relationships at different $\mu_0 H_{\text{dc}}$. When a uniform magnon with a frequency of $f_{\text{ac}} = 10$ GHz is forcefully excited at $\mu_0 H_{\text{dc}} = 20$ mT, as shown in Fig. 1(a1), the magnon splits into two magnons with opposite wave vectors and $f_{\text{ac}}/2$ via three-magnon scattering, as indicated by the red ellipses in Fig. 1(a1). Magnons, which are excited through such a nonlinear-scattering process, are called parametric magnons, in contrast to the normally excited spin waves. Because there are no magnon states with $\theta_k = 15^\circ$ at $\mu_0 H_{\text{dc}} = 20$ mT, the parametric magnons have θ_k^{th} values that are larger than 15° , as shown in Fig. 1(c). When $\mu_0 H_{\text{dc}}$ reaches 80 mT, $f_{\text{ac}}/2$ matches the dispersion relationship for $\theta_k = 15^\circ$, as shown in Fig. 1(a2), where $\mu_0 H_{\text{ac}}^{\text{th}}$ becomes minimal. The further increase in $\mu_0 H_{\text{dc}}$ up to 120 mT causes $f_{\text{ac}}/2$ to approach the bottom of the magnon band, which corresponds to $\theta_k = 0^\circ$, as shown in Fig. 1(a3). Thus, $\mu_0 H_{\text{ac}}^{\text{th}}$ rapidly increases because the denominator of Eq. (4) approaches zero. When $\mu_0 H_{\text{dc}}$ is larger than 120 mT, three-magnon scattering can no longer occur because there are no magnon states at $f_{\text{ac}}/2$. Thus, the butterfly curve in Fig. 1(b) is closely related to the magnon-band structures. From the values of $f_{\text{ac}}/2$ and $\mu_0 H_{\text{dc}}^{\text{div}}$ at which the divergence of $\mu_0 H_{\text{ac}}^{\text{th}}$ appears, we can determine the lowest frequency of the magnon band as $f_{\text{min}}(\mu_0 H_{\text{dc}}^{\text{div}}) = f_{\text{ac}}/2$.

III. EXPERIMENT

In this section, we will show that f_{min} in narrow-shaped NiFe strips can be experimentally obtained by detecting the spin waves excited via the three-magnon scattering process. In Sec. III A, we present the sample configuration and experimental setup; in Sec. III B, the ferromagnetic resonance of the NiFe strips in the linearly responding regime is shown. In Sec. III C, the strong excitation of magnons is examined by applying microwave fields that are stronger than those used in Sec. III B, and magnon modes are successfully detected by measuring the change in the electric resistance of the NiFe strips owing to the AMR effect.

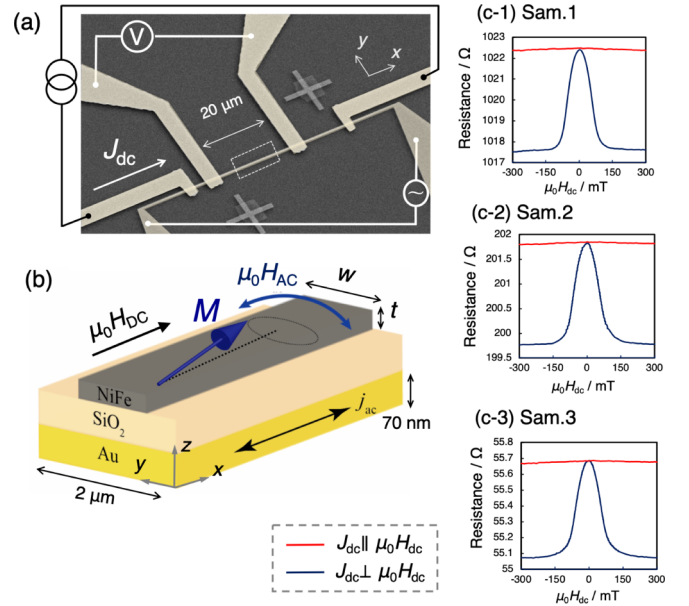


FIG. 2. (a) Scanning electron microscopy image of the sample and setup for the AMR experiment and (b) a schematic enlargement of the dashed square area in (a). A microwave synthesizer applies a continuous microwave to the CPW, which is embedded below the NiFe strip. The dc source and nanovoltmeter are connected to the four terminals, which are attached to the NiFe strip. (c) $\mu_0 H_{\text{dc}}$ dependence of the electric resistance of the NiFe strip for each sample. The red (blue) curve shows the AMR curve of the NiFe strip when $\mu_0 H_{\text{dc}}$ was swept parallel (perpendicular) to the electric current J .

A. Sample preparation and experimental setup

In this section, the sample preparation and our experimental setup are shown. Figure 2(a) shows the scanning electron micrograph of the sample and the experimental setup. A $2\text{-}\mu\text{m}$ -wide coplanar waveguide (CPW) made of Ti(5 nm)/Au(70 nm) was fabricated on the surface-oxidized Si substrate by a conventional liftoff technique using electron-beam lithography and evaporation. Then, three NiFe strips with different dimensions (see Table I) were fabricated. These strips had the aspect ratio t/w fixed at 0.075 but different dimensions with $(w, t) = (400 \text{ nm}, 30 \text{ nm})$, $(800 \text{ nm}, 60 \text{ nm})$, and $(1600 \text{ nm}, 120 \text{ nm})$ for samples 1, 2, and 3, respectively. Finally, four-terminal electrodes composed of Ti(5 nm)/Au(100 nm) were connected to the NiFe strips. The separation distance between the voltage terminals was $20 \mu\text{m}$. By applying a continuous microwave to the CPW using a microwave synthesizer (Anritsu MG3694B), an ac magnetic field $\mu_0 H_{\text{ac}}$ was produced perpendicular to the NiFe strip. The resistance of the NiFe strip was measured by the conventional four-terminal method.

The AMR curves, which were measured by applying a direct current of 0.2 mA in the absence of $\mu_0 H_{\text{ac}}$, are shown in Fig. 2(c) for each NiFe strip. Owing to the AMR effect, the electrical resistance depends on the relative angle φ_0 between the magnetization vector and the current direction (x axis):

$$R(\varphi) = R_{\perp} + (R_{\parallel} - R_{\perp}) \cos^2 \varphi_0. \quad (6)$$

TABLE I. Configurations of the NiFe strips used in the micromagnetic simulation and experiment. Three types of NiFe strips with different dimensions but the same aspect ratio are used. The lengths of the NiFe strips are $10\ \mu\text{m}$ for the simulation and $20\ \mu\text{m}$ for the experiment. Demagnetization factors (N_x, N_y, N_z) are calculated on the basis of the analytical relationship [40]. f_{FMR} and f_{min} , respectively, are the resonant frequency of the FMR and the bottom frequency of the BVW at $\mu_0 H_{\text{dc}} = 20\ \text{mT}$, as expected from the numerical-dispersion relationship in Fig. 8.

Sample	(w, t)	t/w	(N_x, N_y, N_z)	f_{FMR} (GHz)	f_{min} (GHz)
Sample 1	(400 nm, 30 nm)	0.075	(0, 0.10, 0.90)	8.4	6.2
Sample 2	(800 nm, 60 nm)	0.075	(0, 0.10, 0.90)	8.4	4.9
Sample 3	(1600 nm, 120 nm)	0.075	(0, 0.10, 0.90)	8.4	3.8

Here, R_{\perp} and R_{\parallel} are the electrical resistances of the NiFe strip when the magnetization direction is, respectively, perpendicular and collinear to the current direction. The blue and red curves in Fig. 2(c) show R_{\perp} and R_{\parallel} , respectively. When the magnetization precession with a cone angle of φ is excited in the NiFe strip, the magnetization components, which are collinear to the current direction, decrease.

B. Low-power excitation of spin waves

We examined the resonant condition of the NiFe strip in the linearly excited regime (i.e., $\mu_0 H_{\text{ac}} < \mu_0 H_{\text{ac}}^{\text{th}}$) using the vector-network-analyzer FMR (VNA-FMR) measurement. A microwave with an amplitude of $-5\ \text{dBm}$ and a frequency in the range of 1 to 20 GHz was applied to the CPW embedded under the NiFe strip to obtain a microwave-reflection coefficient S_{11} . The inset in Fig. 3 shows an example of the frequency dependence of $\text{Re}[\Delta S_{11}]$ at $\mu_0 H_x = 145\ \text{mT}$, which was measured for sample 2. The rapid decrease in $\text{Re}[\Delta S_{11}]$ is clearly observed at 12.2 GHz, which can be denoted by f_{FMR} at 145 mT. The open circles in Fig. 3 show f_{FMR} as a function of $\mu_0 H_x$, which is measured for each NiFe strip. The dashed lines in Fig. 3 show the lines of best fit according to Eq. (5). The parameters that best match the experiment are $M_s = 0.91\ \text{T}$ and $(N_x, N_y, N_z) = (0, 0.11, 0.89)$. We also determined the Gilbert damping constant $\alpha = 0.0095 \pm 0.0002$ from the

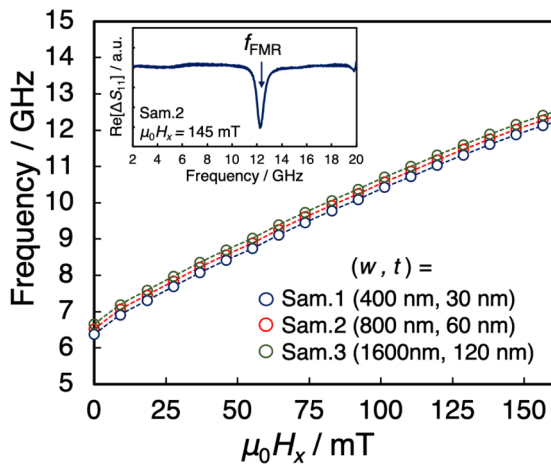


FIG. 3. The $\mu_0 H_x$ dependence of f_{FMR} for each NiFe strip measured by the VNA-FMR technique. The inset shows an example of the f_{ac} dependence of $\text{Re}[\Delta S_{11}]$ at $\mu_0 H_{\text{dc}} = 145\ \text{mT}$ for sample 2. A clear dip appears at $f_{\text{ac}} = 12.2\ \text{GHz}$, which we denote as f_{FMR} . The dashed lines are the lines of best fit calculated by Eq. (5).

full width at half maximum. These values are consistent with the previously reported values for NiFe [37].

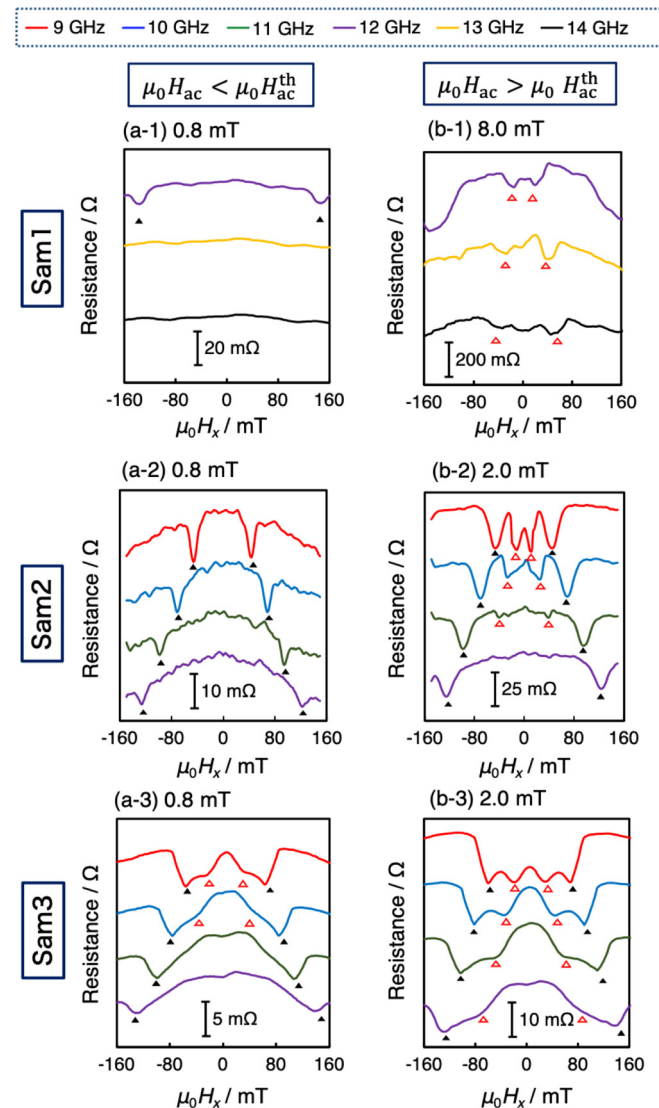


FIG. 4. AMR curves for each sample measured while applying $\mu_0 H_{\text{ac}}$ with a frequency in the range from 9 to 14 GHz when (a) $\mu_0 H_{\text{ac}} < \mu_0 H_{\text{ac}}^{\text{th}}$ and (b) $\mu_0 H_{\text{ac}} > \mu_0 H_{\text{ac}}^{\text{th}}$ for samples 1 to 3. When the magnetization precession was excited, the electric resistance of the NiFe strips decreased. The solid black triangles show the FMR modes, and the open red triangles show the parametric magnons excited via the three-magnon scattering process.

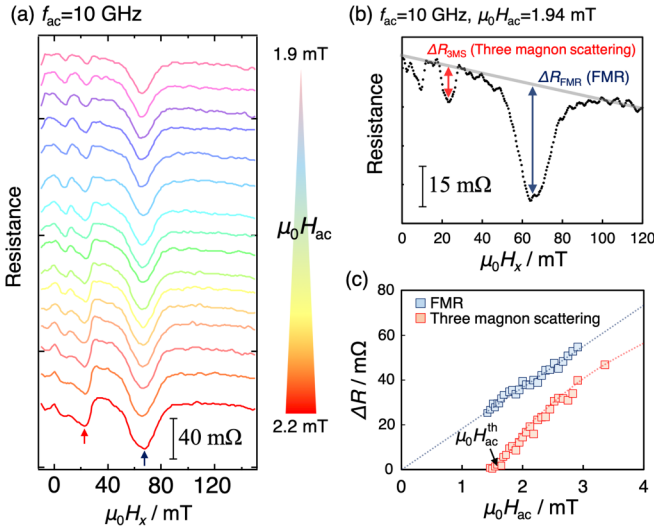


FIG. 5. (a) Transition of the AMR curves under various $\mu_0 H_{ac}$ measured for sample 2. The dips indicated by the blue and red arrows correspond to the excitation of the FMR and three-magnon scattering, respectively. (b) Definition of ΔR for the two resonant modes. (c) $\mu_0 H_{ac}$ dependence of ΔR for the FMR and three-magnon scattering mode. $\mu_0 H_{ac}^{th}$ is defined by the value of $\mu_0 H_{ac}$ at which ΔR begins to increase from zero.

C. High-power excitation of spin waves

In this section, we will show the results of a strong magnon excitation. By applying continuous microwave radiation with an amplitude larger than -5 dBm, the higher-order spin waves, which were not detected by the previous VNA-FMR measurement, were observed. The initially excited magnons with a frequency of f_{ac} are laterally quantized in each NiFe strip with a wave number determined by the width of the strips, i.e., $k_y = \frac{\pi}{w}$ [35]. Figures 4(a2) and 4(b2) show the $\mu_0 H_{dc}$ dependence of the resistance of sample 2 measured with f_{ac} ranging from 9 to 12 GHz. As shown in Fig. 4(a2), when $\mu_0 H_{ac} = 0.8$ mT, only one mode, which is indicated by solid black triangles, appeared at each frequency. This mode is attributable to the FMR mode by comparison with the resonant condition in Fig. 3. When $\mu_0 H_{ac}$ is increased to 2.0 mT, additional dips appear in the lower field at f_{ac} in the range from 9 to 11 GHz (indicated by open red triangles). As shown later in this section, the additional modes appear when the amplitude of $\mu_0 H_{ac}$ exceeds a threshold value. This threshold behavior is a characteristic feature of magnons excited via three-magnon scattering. Similarly, AMR curves were measured for sample 1 at $\mu_0 H_{ac} = 0.8$ mT [Fig. 4(a1)] and $\mu_0 H_{ac} = 8.0$ mT [Fig. 4(b1)] and for sample 3 at $\mu_0 H_{ac} = 0.8$ mT [Fig. 4(a3)] and $\mu_0 H_{ac} = 2.0$ mT [Fig. 4(b3)]. The comparison of $\mu_0 H_{ac}^{th}$ amplitudes required to excite three-magnon scattering showed that three-magnon scattering can occur via smaller $\mu_0 H_{ac}$ for thicker NiFe strips. As shown in Fig. 4, the resonant fields for FMR and three-magnon scattering (solid black and open red triangles, respectively) are closer to each other in thicker NiFe strips. According to Eq. (4), $\mu_0 H_{ac}^{th} \propto 1 - (f_{FMR}/f_{ac})^2$, such that $\mu_0 H_{ac}^{th}$ is smaller for the thicker NiFe strip, in which the value of f_{FMR}/f_{ac} is close to unity. Indeed, as shown later in Sec IV, our numerical

result for the dispersion relationships for the NiFe strips in Fig. 8 is also consistent with this experimental behavior.

The amplitude of $\mu_0 H_{ac}^{th}$ for three-magnon scattering is discussed. Here, we focus on the results for sample 2 because it is difficult to separate the FMR and three-magnon scattering modes in sample 3, as shown in Fig. 4(b3). Moreover, for sample 1, an excessive increase in the microwave is needed to realize the three-magnon scattering, although the frequency that appears in the three-magnon scattering mode can be much higher than the FMR frequency. Figure 5(a) shows the transition of the AMR curves at $f_{ac} = 10$ GHz with an increase in the $\mu_0 H_{ac}$ amplitude from 1.9 to 2.2 mT with an interval of 0.02 mT. As shown in Fig. 5(b), three dips appear at $\mu_0 H_{dc} = 7, 21,$ and 72 mT when $\mu_0 H_{ac} = 1.9$ mT. The dip at $\mu_0 H_{dc} = 72$ mT corresponds to the FMR mode. The amplitudes of the two dips, which appear in the fields below 72 mT, increased with $\mu_0 H_{ac}$, before finally merging. We define the decreases in electrical resistance owing to FMR and spin waves as ΔR_{FMR} and ΔR_{3MS} , respectively, as shown in Fig. 5(b). Then, the spin wave modes are found to be excited via three-magnon scattering. Blue and red squares in Fig. 5(c) show ΔR_{FMR} and ΔR_{3MS} , respectively, as a function of $\mu_0 H_{ac}$. The lower field mode appeared when $\mu_0 H_{ac} > 1.60$ mT, and ΔR_{FMR} increased linearly with $\mu_0 H_{ac}$. We define the value of $\mu_0 H_{ac}$ at which ΔR_{3MS} becomes nonzero, e.g., $\mu_0 H_{ac}^{th} = 1.60$ mT, in Fig. 5(c). The existence of the $\mu_0 H_{ac}$ threshold amplitude needed to excite the lower field mode is the evidence that spin waves are excited via the three-magnon scattering process.

Figure 6(a) shows the $\mu_0 H_x$ dependence of $\mu_0 H_{ac}^{th}$ (i.e., the butterfly curve) measured for sample 2. When $f_{ac} = 9$ GHz, $\mu_0 H_{ac}^{th}$ shows a broad flat minimum with fine structures in the field range between 12 and 15 mT and then rapidly increases at a divergence field $\mu_0 H_{dc}^{div}$ of approximately 18 mT. Similar results were obtained for other f_{ac} . We can evaluate f_{min} at a given magnetic field $\mu_0 H_x$ from the butterfly curve shown in Fig. 6(a). Because $\mu_0 H_{ac}^{th}$ shows a finite value below $\mu_0 H_{dc}^{div}$, the region where $\mu_0 H_x < 18$ mT qualitatively corresponds to the situation shown in Figs. 1(a1) and 1(a2). Then, at the divergent field $\mu_0 H_{dc}^{div}$, the condition that $f_{ac}/2 = f_{min}(\mu_0 H_x)$ is satisfied. Thus, we can determine f_{min} at $\mu_0 H_{dc}^{div}$. Blue open circles in Fig. 6(b) show f_{min} as a function of $\mu_0 H_x$, as evaluated from the butterfly curves in Fig. 6(a). As shown later in Sec. IV B, these experimental results are quantitatively consistent with the numerical results (red open squares) in Fig. 6(b).

In contrast, some temperature increase is expected in the three-magnon scattering experiments [Fig. 4(b)] because the microwave applied to the antenna is much stronger than that in the VNA-FMR experiments (Fig. 3). The temperature increase in sample 1 is the largest among the three samples because of the largest applied $\mu_0 H_{ac}$. Indeed, the asymmetric resonant field is prominent in Fig. 4(b1). This temperature increase causes a decrease in M_s which leads to a decrease in resonant frequencies. However, the heating effect on the resonant frequency of three-magnon scattering modes is negligible because the experimental results are consistent with the resonant frequency of the three-magnon scattering modes, which are calculated in the numerical simulation without considering any sample heating (see the Appendix).

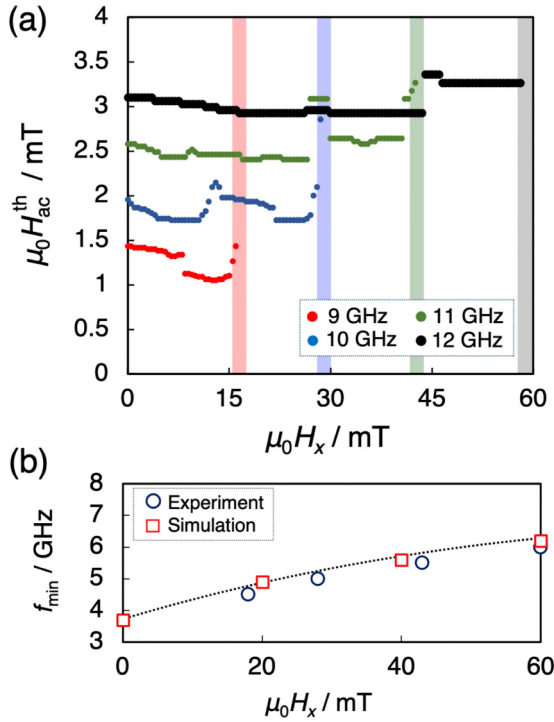


FIG. 6. (a) Butterfly curves measured for sample 2 at frequencies of 9 to 12 GHz. The shaded area shows a certain magnetic field at which $\mu_0 H_{ac}^{th}$ diverges, which yields the divergent field $\mu_0 H_{dc}^{div}$. (b) $\mu_0 H_x$ dependence of f_{min} . Blue open circles represent the experimental results, and red open squares are the values obtained from the simulated dispersion relationship in Fig. 8(a2). The dashed line serves as a guide for the eyes.

Figure 7 shows resonant frequencies for the FMR (open circles) and the three-magnon scattering (open squares) modes as a function of $\mu_0 H_x$. The f_{FMR} values measured using the VNA-FMR technique are also shown as the solid curves. The three NiFe strips in Fig. 7 show completely different

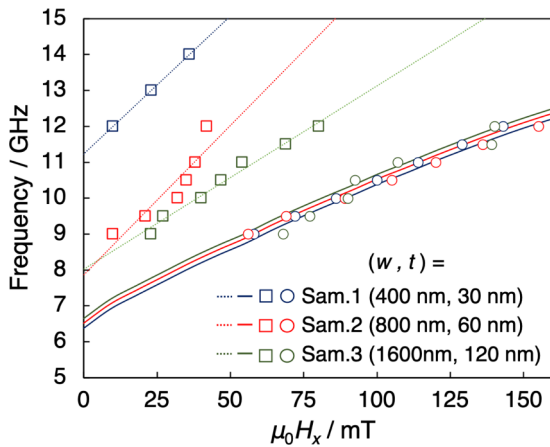


FIG. 7. Resonant frequencies of the FMR (open circles) and spin wave (open squares) modes. The solid line shows the FMR condition measured using the VNA-FMR technique. The dashed lines serve as a guide for the eyes for the spin wave modes excited via three-magnon scattering.

resonant frequencies for three-magnon scattering at a given $\mu_0 H_x$, although those f_{FMR} are approximately the same. In the following section, the dispersion relationships of narrow NiFe strips and their detailed strip size dependence will also be discussed.

IV. MICROMAGNETIC SIMULATION

We conducted a micromagnetic simulation using MUMAX3 [38]. The thickness t and width w of the NiFe strips ranged from 30 to 120 nm and from 200 to 1600 nm, respectively. The lengths of the NiFe strips were fixed at 10 μm . The saturation magnetization, exchange-stiffness constant, and the Gilbert damping coefficient were set to $M_s = 0.90$ T, $A_{ex} = 1.3 \times 10^{-11}$ J/m, and $\alpha = 0.01$, respectively, and thermal agitation at 300 K was assumed. The numerical grid had dimensions of $5 \times 5 \times 5$ nm³, with a side length comparable to the exchange length l_{ex} of NiFe (5.7 nm) [39]. The eigenfrequency of the magnon excited in the NiFe strip is obtained via a fast-Fourier-transform (FFT) analysis of the temporal evolution of the y component of the magnetic moment m_y located at the center of the strip. Conversely, the magnon number $\langle n_{mag} \rangle$ is calculated via the time averaging of the volume-averaged magnetization component M_x along the long axis of the strip.

A. Dispersion relationship for the BVW mode

First, the $\mu_0 H_{dc}$ dependence of f_{min} is examined by calculating the dispersion relationship for these modes. The magnetization precession caused by the application of the temporally and spatially varying magnetic field

$$\mu_0 \mathbf{H}(k_x, f_{ac}) = \mu_0 H_{dc} \begin{bmatrix} \cos(0.1^\circ) \\ \sin(0.1^\circ) \\ 0 \end{bmatrix} + \mu_0 H_{ac} \begin{bmatrix} 0 \\ \sin(k_x x) \sin(2\pi f_{ac} t) \\ 0 \end{bmatrix} \quad (7)$$

was simulated. The magnetic field given by Eq. (7) preferentially excites magnons with a wave number k_x and frequency f_{ac} . Because $\mu_0 \mathbf{H}(k_x, f_{ac})$ is modulated only along the x axis, the obtained dispersion relationship corresponds to the BVW modes. Here, $\mu_0 H_{ac} = 1.0$ mT, and the rise time was set to zero. f_{ac} and k_x were varied from 3 to 10 GHz and from 1 to 90 rad/ μm , respectively. By calculating the amplitude of the temporally oscillating magnetization component in the interval from 9 to 10 ns after the $\mu_0 \mathbf{H}(k_x, f_{ac})$ application commenced, $\langle n_{mag} \rangle$ could be evaluated. Figure 8(a) shows a color plot of $\langle n_{mag} \rangle$ as a function of k_x and f_{ac} when $\mu_0 H_x = 20$ mT. The bright contrast corresponds to the condition when the BVW modes are resonantly excited. f_{min} is located at approximately $k_x = 20$ μm^{-1} for all NiFe strips. To compare it with the experimental $\mu_0 H_x$ dependence of f_{min} , the f_{min} value obtained from the simulated dispersion relationship is shown by red open squares in Fig. 6(b). The consistency between the experiment and simulation clearly suggests that f_{min} can be measured by detecting three-magnon scattering. In addition, we confirmed that the simulated dispersion relationship in Fig. 8(a) can quantitatively explain the numerical

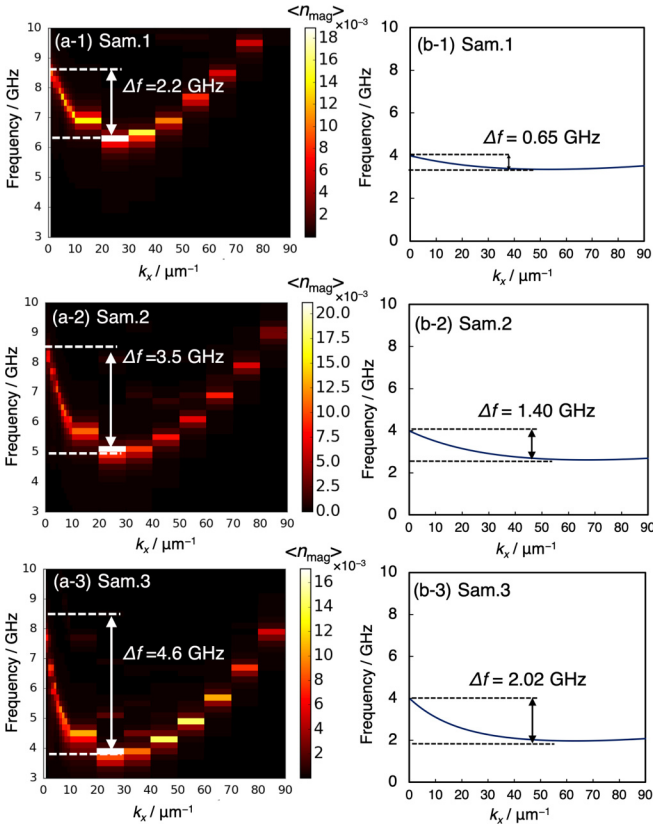


FIG. 8. Color plot of $\langle n_{\text{mag}} \rangle$ as a function of the wave number k_x along the strip and the frequency calculated for the NiFe strips with (w, t) of (a1) (400 nm, 30 nm), (a2) (800 nm, 60 nm), and (a3) (1600 nm, 120 nm). The aspect ratio t/w of the NiFe strip is fixed at 0.075 for (a1), (a2), and (a3). Bright contrast shows the magnon excitation condition, which corresponds to the spin wave dispersion relationship. For comparison, the spin wave dispersion relationships obtained from the analytical solutions given by Eqs. (1)–(3), which are generally used for the thin-film limit, are shown in (b1), (b2), and (b3), where the thickness of the NiFe is the same as that in (a1), (a2), and (a3), respectively.

resonant conditions of parametric magnons generated via three-magnon scattering, as described in the Appendix. It was also confirmed that the dispersion relationship in narrow strips had a completely different structure than that for the thin-film-limit case. Figures 8(b1)–8(b3) show the dispersion relationships calculated from Eq. (1) for $t = 30, 60,$ and 120 nm, respectively, when $\mu_0 H_x = 20$ mT. However, there was a larger variation in Δf as a function of w and t in narrow-shaped strips [Fig. 8(a)] than that for the thin-film-limit case [Fig. 8(b)]. This characteristic suggests that narrow ferromagnetic strips have low resonance frequency for the BVW mode, whereas they show strong coercivity owing to the strong shape anisotropy, which enables spin wave excitation without an external magnetic field.

The low f_{min} for the narrow NiFe strip is attributable to the aspect ratio dependence of dipole-interaction energy. For simplicity, we consider NiFe with two limit cases, i.e., $t/w = 0$ (thin-film limit) and $t/w = 1$ (strip). In the limit of $t/w = 0,$

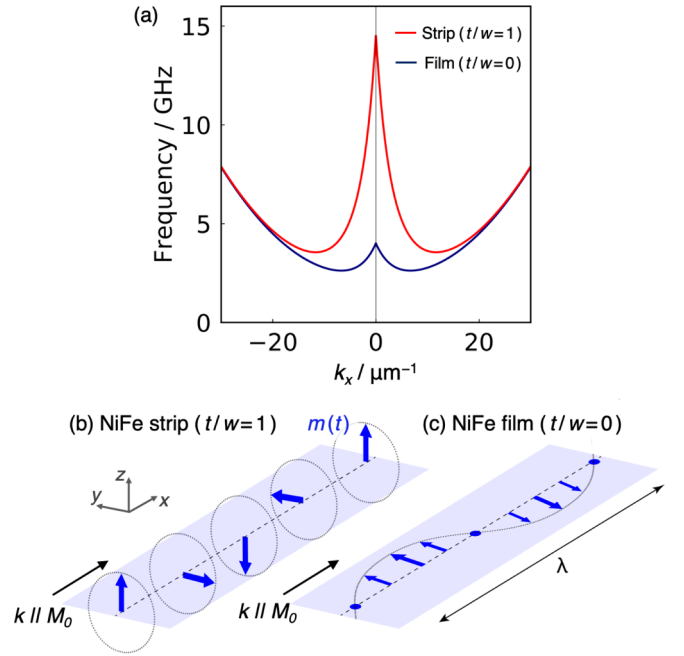


FIG. 9. (a) Spin wave dispersion relationship for the BVW modes calculated for the NiFe strip (red curve) and NiFe film (blue curve) with $t = 60$ nm at $\mu_0 H_x = 20$ mT. (b) and (c) Schematic magnetic configurations of the BVW mode propagating along the static magnetization direction M_0 . Blue arrows show the dynamic component of magnetization $m(t)$ for the (b) strip and (c) thin film.

f_{FMR} is given by

$$f_{\text{FMR}} = \frac{\gamma}{2\pi} \sqrt{\mu_0 H_{\text{dc}} [\mu_0 H_{\text{dc}} + M_s]}, \quad (8)$$

whereas in the limit of $t/w = 1,$

$$f_{\text{FMR}} = \frac{\gamma}{2\pi} \left[\mu_0 H_{\text{dc}} + \frac{M_s}{2} \right]. \quad (9)$$

When $t/w = 1,$ the dipole interaction should be considered along the y and z axes, equivalently. Similar to $f_{\text{FMR}},$ the dispersion relationship for the BVW mode in the strip with $t/w = 1$ can be expected from Eq. (1) as

$$f = \frac{\gamma}{2\pi} \left[\mu_0 H_{\text{dc}} + \frac{2A}{M_s} k^2 + \frac{M_s F_p(kt)}{2} \right]. \quad (10)$$

Red and blue solid curves in Fig. 9(a) show the dispersion relationships calculated using Eqs. (10) and (1), respectively. As shown in Fig. 9(a), when the dipole interaction becomes isotropic between the y and z axes, Δf considerably increases. This increase in Δf can be qualitatively understood from the shape dependence of the ellipticity of the dynamic component of magnetization $m(t)$. Figures 9(b) and 9(c) show the schematic configuration of the dynamic component of magnetization for $t/w = 1$ and $0,$ respectively. Owing to the shape anisotropy, $m(t)$ exhibits a circular orbit in Fig. 9(b) and a highly elliptical orbit in Fig. 9(c). The isotropic precession of magnetization, which appeared in the strip, promotes the decrease in the dipole-interaction energy owing to the spin wave excitation, which is expressed by $F_p(kt)$ in Eqs. (1) and (10). Consequently, f_{min} can be considerably decreased from f_{FMR} when t/w increases.

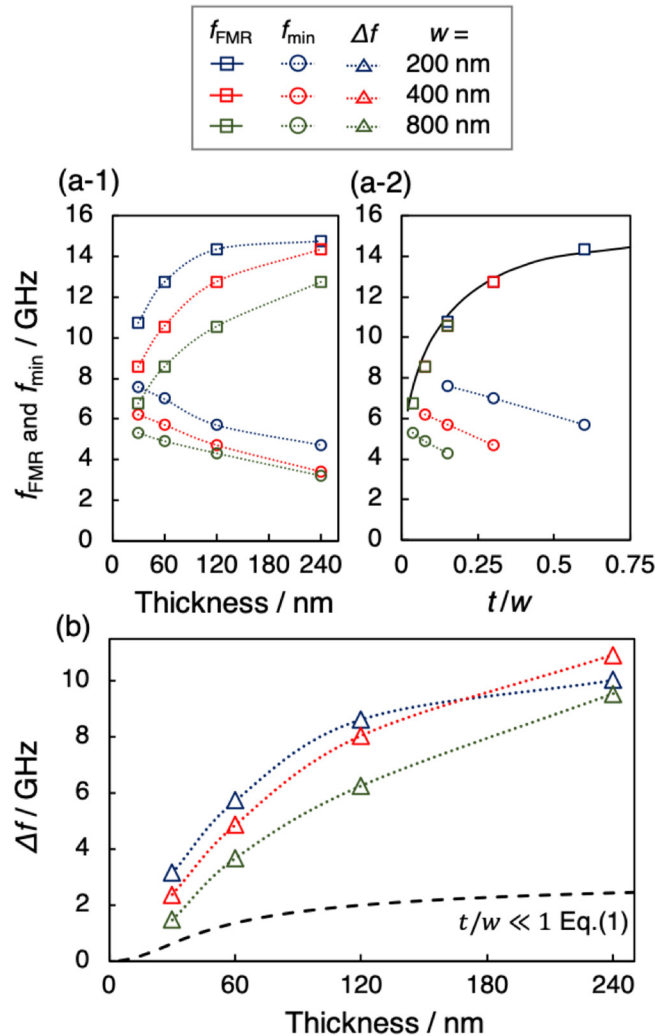


FIG. 10. (a) f_{FMR} (open squares) and f_{min} (open circles) as a function of (a1) t and (a2) t/w for the NiFe strips with $w = 200$, 400, and 800 nm. The solid curve in (a2) shows the f_{FMR} calculated using the Kittel relationship of Eq. (5). (b) Δf as a function of t . The dashed line shows Δf calculated from Eq. (1).

B. Size dependence of the magnon bandwidth

Finally, we will discuss the size dependence of Δf . Figure 10(a) shows the f_{FMR} (open squares) and f_{min} (open circles) values for the NiFe strips with different values of w as functions of t and t/w , respectively. f_{FMR} was obtained via the FFT analysis of the magnetization relaxation process, which slightly deviated from its equilibrium direction at $\mu_0 H_x = 20$ mT. As shown in Fig. 10(a1), f_{min} decreased with t , whereas f_{FMR} increased, which resulted in the increase in Δf with t . Open triangles in Fig. 10(b) show the t dependence of Δf , and the black dashed line shows Δf , which was calculated using Eq. (1) by assuming that $t/w \ll 1$. It was determined that the variation range of Δf in narrow NiFe strips is larger than that in the film-limit case by a degree of magnitude. Figure 10(a2) shows f_{FMR} and f_{min} as a function of t/w . It is observed that f_{FMR} does not depend on w or t but on their aspect ratio t/w . However, f_{min} depends on the absolute values of w or t . Here, the black solid curve

shows f_{FMR} , which was calculated on the basis of Eq. (5). The obtained value is in good agreement with the simulation results. N_i in Eq. (5) was obtained from w and t using the analytical relationship [40]. These features enable us to independently vary f_{FMR} , f_{min} , and, consequently, Δf over a wide range. Thick and narrow ferromagnetic strips offer considerable advantages for designing integrated magnonic devices and for systematically studying BEC of magnons.

V. CONCLUSION

In this paper, we demonstrated that the magnon bandwidth ($\Delta f = f_{\text{FMR}} - f_{\text{min}}$) can be significantly increased in narrow NiFe strips with magnon-band structures that are difficult to solve analytically. Three-magnon scattering was successfully observed in 20- μm -long NiFe strips with three different dimensions of $(w, t) = (400 \text{ nm}, 30 \text{ nm})$, $(800 \text{ nm}, 60 \text{ nm})$, and $(1600 \text{ nm}, 120 \text{ nm})$ but with fixed aspect ratio t/w of 0.075. We examined the magnon bandwidth from the three-magnon scattering spectra by measuring the AMR effect in the NiFe strips. When the microwave field was stronger than a certain threshold amplitude, the spin wave mode was observed in addition to the FMR. The resonant frequencies of the spin wave mode are widely scattered among the three NiFe strips, although the FMR frequencies are almost identical. A comparison with the micromagnetic simulation results confirmed that the spin wave mode may be attributed to three-magnon scattering. This consistency supports the experimental scheme by which we can evaluate f_{FMR} and f_{min} and hence Δf .

A ferromagnetic strip with a large shape anisotropy, which is significant for the dense integration of magnon circuits, enables spin wave excitation under zero magnetic field. A large decrease occurs more fluently, which enables us to excite many magnons with a small $\mu_0 H_{\text{ac}}$. Furthermore, the magnon bandwidth and propagation velocity of the spin wave can easily be tuned by changing the t and w values of the ferromagnetic strip.

ACKNOWLEDGMENTS

This work was supported by the Advanced Storage Research Consortium (ASRC) and JSPS KAKENHI Grant No. 18H03867. G.O. is supported by JSPS through a research fellowship for young scientists (Grant No. 18J20062).

APPENDIX: EXTERNAL FIELD DEPENDENCE OF THE RESONANT FREQUENCY OF THE SPIN WAVE

For clarity, the spin wave spectra, which were excited via three-magnon scattering, will be shown, and the magnon frequency for each resonant mode will be addressed. Figure 11(a) shows the temporal evolution of M_x/M_s as calculated for the three strips with different w and t values. Here, $\mu_0 H_{\text{ac}}$ was applied for a duration of 50 ns. The time-averaged value of M_x/M_s between 45 and 50 ns was used to evaluate the magnon numbers, $\langle n_{\text{mag}} \rangle = 1 - \langle M_x/M_s \rangle$, because the temporal variation of $\langle n_{\text{mag}} \rangle$ owing to the transient of a nonequilibrium magnetization dynamics can be neglected. Color plots of $\langle n_{\text{mag}} \rangle$ as a function of $\mu_0 H_x$ and f_{ac} are shown in Figs. 11(b) and 11(c), which correspond to the

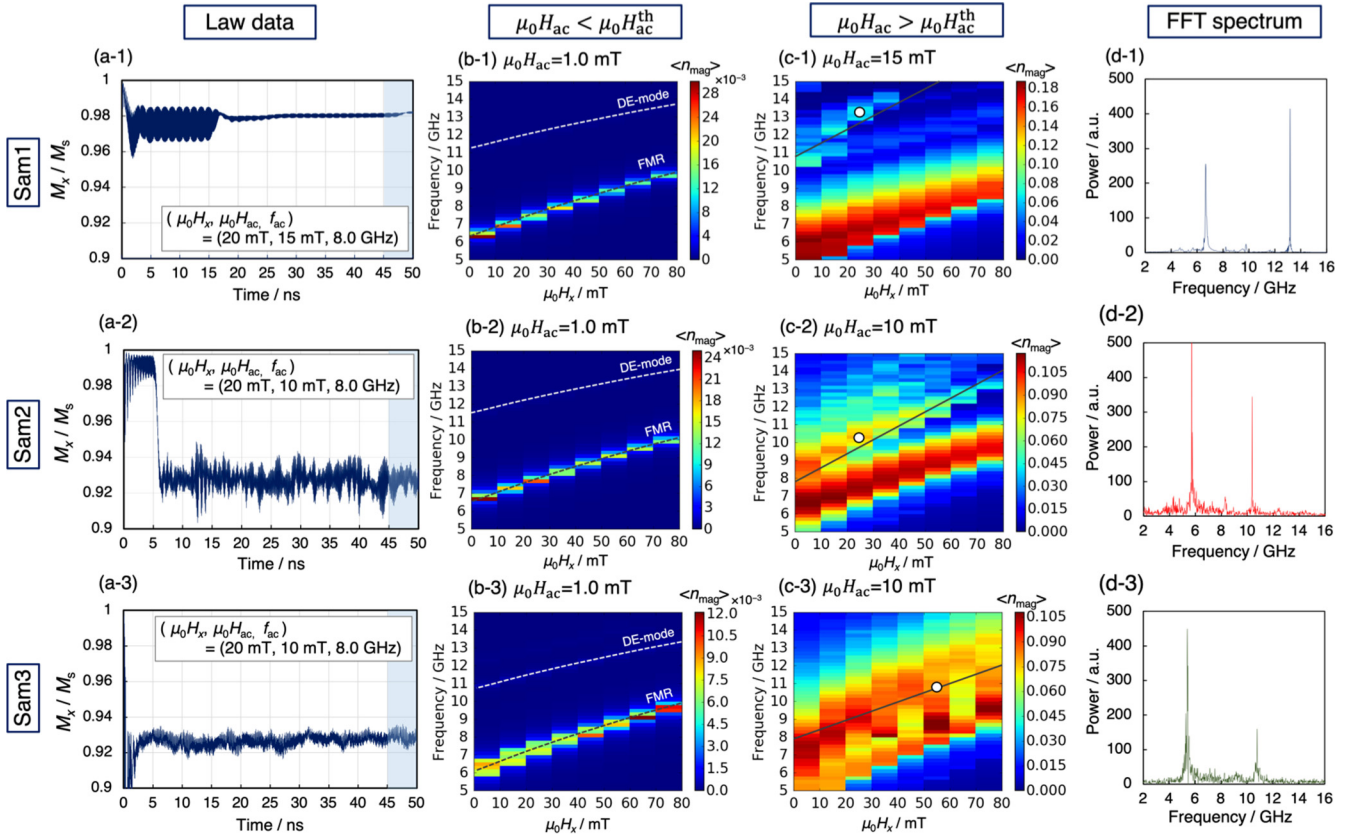


FIG. 11. Results of the micromagnetic simulation. (a) Examples of the temporal development of M_x/M_s over 50 ns for (a1) sample 1 to (a3) sample 3. $\mu_0 H_{dc}$ and f_{ac} dependence of the magnon number n_{mag} when (b) $\mu_0 H_{ac} < \mu_0 H_{ac}^{th}$ and (c) $\mu_0 H_{ac}^{th} < \mu_0 H_{ac}$. (d) Magnon frequency spectra obtained from the FFT analysis, which was applied to the temporal development of the m_y component for the unit cell at the center of the NiFe strip. The FFT spectra were calculated at the condition marked by the open circles in (c).

weak- and strong-excitation regimes, respectively. Red shows the condition under which the large-angle precession, i.e., many magnons, is excited. Figure 11(b) shows a color plot of $\langle n_{mag} \rangle$ as a function of $\mu_0 H_x$ and the frequency at which $\mu_0 H_{ac} < \mu_0 H_{ac}^{th}$. Two resonant modes of frequencies (i.e., 6.0 and 11.2 GHz) appear at zero magnetic field for all NiFe strips. The lower-frequency mode is attributed to the FMR. It is noted that the higher-frequency mode is not excited via the three-magnon scattering process because the applied $\mu_0 H_{ac}$ is too small to excite the three-magnon scattering. Indeed, we confirmed that the higher-frequency mode is attributable to the Damon-Eshbach (DE) mode from the magnetization distribution of the excited-spin wave mode. Figure 11(c) shows a color plot of $\langle n_{mag} \rangle$ as a function of $\mu_0 H_x$ and the frequency calculated for the condition at which $\mu_0 H_{ac} > \mu_0 H_{ac}^{th}$. As shown in Fig. 11(c), a resonant mode other than FMR or DE appears. In addition, the resonant frequencies of the spin wave mode, which are shown in Fig. 11(c), are different for the three NiFe strips with different dimensions. For comparison with the experimental resonant conditions, the dashed lines in Fig. 7 are shown in Fig. 11(c). Clearly, there is a strong contrast, i.e., large $\langle n_{mag} \rangle$, around the experimental resonant condition. For sample 2, as shown in Fig. 8(a2), f_{min} is

4.9 GHz at $\mu_0 H_{dc} = 20$ mT. Therefore, the spin wave modes excited via three-magnon scattering may appear when $f_{ac} > 9.8$ GHz. Indeed, as shown in Fig. 11(c2), many magnons are excited at approximately 10.2 GHz when $\mu_0 H_{dc} = 20$ mT is applied. Similarly, as shown in Fig. 11(c1) for sample 1 and Fig. 11(c3) for sample 3, three-magnon scattering excited spin wave modes were confirmed to appear when $f_{ac} > 2f_{min}$. The consistency between the experimental and simulated results supports the scheme to evaluate f_{min} by measuring resonant conditions, as shown in Fig. 7.

In the three-magnon scattering process, the $f_{ac}/2$ magnons are excited in addition to f_{ac} magnons. Specifically, we can determine whether the spin wave mode is excited via three-magnon scattering from the spin wave precession frequency. We applied the FFT analysis to the temporal development of m_y , which is located at the center of the NiFe strip, to confirm the frequency of the magnetization precession, which was calculated at the magnon frequency. Figure 11(d) shows the power spectra, which were calculated for the condition indicated by the open circles in Fig. 11(c). In all NiFe strips, peak signals appear at $f_{ac}/2$ and at f_{ac} . The results clearly suggest that the experimentally observed additional resonant mode in Fig. 7(c) is excited by the three-magnon scattering process.

[1] A. A. Serga, A. V. Chumak, and B. Hillebrands, *J. Phys. D* **43**, 264002 (2010).

[2] A. V. Chumak, V. I. Vasyuchka, A. A. Serga, and B. Hillebrands, *Nat. Phys.* **11**, 453 (2015).

- [3] S. O. Demokritov and A. N. Slavin, *Magnonics: From Fundamentals to Applications* (Springer, Berlin, 2013).
- [4] A. Khitun, M. Bao, and K. L. Wang, *J. Phys. D* **43**, 264005 (2010).
- [5] T. Schneider, *Appl. Phys. Lett.* **92**, 022505 (2008).
- [6] N. Sato, K. Sekiguchi, and Y. Nozaki, *Appl. Phys. Express* **6**, 063001 (2013).
- [7] S. Klingler, P. Pirro, T. Brächer, B. Leven, B. Hillebrands, and A. V. Chumak, *Appl. Phys. Lett.* **106**, 212406 (2015).
- [8] M. Balynskiy, H. Chiang, D. Gutierrez, A. Kozhevnikov, Y. Filimonov, and A. Khitun, *J. Appl. Phys.* **123**, 144501 (2018).
- [9] S. Klingler, P. Pirro, T. Brächer, B. Leven, B. Hillebrands, and A. V. Chumak, *Appl. Phys. Lett.* **105**, 152410 (2014).
- [10] T. Fischer, M. Kewenig, D. A. Bozhko, A. A. Serga, I. I. Syvorotka, F. Ciubotaru, C. Adelman, B. Hillebrands, and A. V. Chumak, *Appl. Phys. Lett.* **110**, 152401 (2017).
- [11] O. Rousseau, B. Rana, R. Anami, M. Yamada, K. Miura, S. Ogawa, and Y. Otani, *Sci. Rep.* **5**, 9873 (2015).
- [12] N. Kanazawa, T. Goto, K. Sekiguchi, A. B. Granovsky, C. A. Ross, H. Takagi, Y. Nakamura, and M. Inoue, *Sci. Rep.* **6**, 30268 (2016).
- [13] M. H. Ahmed, J. Jeske, and A. D. Greentree, *Sci. Rep.* **7**, 41472 (2017).
- [14] A. V. Chumak, A. A. Serga, and B. Hillebrands, *Nat. Commun.* **5**, 4700 (2014).
- [15] M. Balinskiy, H. Chiang, and A. Khitun, *AIP Adv.* **8**, 056628 (2018).
- [16] K. Vogt, F. Y. Fradin, J. E. Pearson, T. Sebastian, S. D. Bader, B. Hillebrands, A. Hoffmann, and H. Schultheiss, *Nat. Commun.* **5**, 3727 (2014).
- [17] S. Dutta, S.-C. Chang, N. Kani, D. E. Nikonov, S. Manipatruni, I. A. Young, and A. Naeemi, *Sci. Rep.* **5**, 9861 (2015).
- [18] Q. Wang, P. Pirro, R. Verba, A. Slavin, B. Hillebrands, and A. V. Chumak, *Sci. Adv.* **4**, e1701517 (2018).
- [19] S. O. Demokritov, V. E. Demidov, O. Dzyapko, G. A. Melkov, A. A. Serga, B. Hillebrands, and A. N. Slavin, *Nature (London)* **443**, 430 (2006).
- [20] V. E. Demidov, O. Dzyapko, M. Buchmeier, T. Stockhoff, G. Schmitz, G. A. Melkov, and S. O. Demokritov, *Phys. Rev. Lett.* **101**, 257201 (2008).
- [21] A. A. Serga, V. S. Tiberkevich, C. W. Sandweg, V. I. Vasyuchka, D. A. Bozhko, A. V. Chumak, T. Neumann, B. Obry, G. A. Melkov, A. N. Slavin, and B. Hillebrands, *Nat. Commun.* **5**, 3452 (2014).
- [22] D. A. Bozhko, A. A. Serga, P. Clausen, V. I. Vasyuchka, F. Heussner, G. A. Melkov, A. Pomyalov, V. S. L'vov, and B. Hillebrands, *Nat. Phys.* **12**, 1057 (2016).
- [23] D. A. Bozhko, P. Clausen, G. A. Melkov, V. S. L'vov, A. Pomyalov, V. I. Vasyuchka, A. V. Chumak, B. Hillebrands, and A. A. Serga, *Phys. Rev. Lett.* **118**, 237201 (2017).
- [24] A. J. E. Kreil, D. A. Bozhko, H. Y. Musiienko-Shmarova, V. I. Vasyuchka, V. S. L'vov, A. Pomyalov, B. Hillebrands, and A. A. Serga, *Phys. Rev. Lett.* **121**, 077203 (2018).
- [25] S. Takei and Y. Tserkovnyak, *Phys. Rev. Lett.* **112**, 227201 (2014).
- [26] C. Sun, T. Nattermann, and V. L. Pokrovsky, *J. Phys. D* **50**, 143002 (2017).
- [27] G. Gubbiotti, S. Tacchi, M. Madami, G. Carlotti, A. O. Adeyeye, and M. Kostylev, *J. Phys. D* **43**, 264003 (2010).
- [28] B. Lenk, H. Ulrichs, F. Garbs, and M. Münzenberg, *Phys. Rep.* **507**, 107 (2011).
- [29] M. Krawczyk and D. Grundler, *J. Phys. Condens. Matter* **26**, 123202 (2014).
- [30] A. V. Chumak, A. A. Serga, and B. Hillebrands, *J. Phys. D* **50**, 244001 (2017).
- [31] S. Y. An, P. Krivosik, M. A. Kraemer, H. M. Olson, A. V. Nazarov, and C. E. Patton, *J. Appl. Phys.* **96**, 1572 (2004).
- [32] B. A. Kalinikos and A. N. Slavin, *J. Phys. C* **19**, 7013 (1986).
- [33] P. E. Wigen, *Nonlinear Phenomena and Chaos in Magnetic Materials* (World Scientific, Singapore, 1994).
- [34] A. G. Gurevich and G. A. Melkov, *Magnetization Oscillations and Waves* (CRC Press, Boca Raton, FL, 1996).
- [35] B. Hillebrands and K. Ounadjela, *Spin Dynamics in Confined Magnetic Structures* (Springer, Berlin, 2001), Vol. 1.
- [36] D. D. Stancil and Prabhakar, *Spin Waves: Theory and Applications* (Springer, New York, 2009).
- [37] G. Okano and Y. Nozaki, *Phys. Rev. B* **97**, 014435 (2018).
- [38] A. Vansteenkiste, J. Leliaert, M. Dvornik, M. Helsen, F. G. Sanchez, and B. V. Waeyenberge, *AIP Adv.* **4**, 107133 (2014).
- [39] G. S. Abo, Y. K. Hong, J. Park, J. Lee, W. Lee, and B. C. Choi, *IEEE Trans. Magn.* **49**, 4937 (2013).
- [40] A. Aharoni, *J. Appl. Phys.* **83**, 3432 (1998).